Detection of Simulated Inflicted Metaphyseal Fractures in a Fetal Pig Model: Image Optimization and Dose Reduction with Computed Radiography[1]

Patricia L. Kleinman, MPH
David Zurakowski, PhD
Keith J. Strauss, MSc
Robert H. Cleveland, MD
Jeannette M. Perez-Rosello, MD
David P. Nichols, AM
Kelly H. Zou, PhD
Paul K. Kleinman, MD

Purpose: To prospectively determine in a fetal pig model whether diagnostic performance comparable to that of high-detail screen-film imaging can be achieved with computed radiography for the detection of simulated classic metaphyseal lesions (CMLs), by using Faxitron digital images as the reference standard, and whether radiation dose reduction is possible.

Materials and Methods: This study was granted exempt status by the institutional review board and the animal care and use committee. Fractures simulating the CML were produced in distal femurs of 20 deceased fetal pigs. Twenty normal femurs served as control femurs. Femurs were imaged with a standard single-side–read 100-μm pixel sampling imaging plate (IP), a high-resolution dual-side–read 50-μm pixel sampling IP, and a high-detail screen-film imaging system. Eight tube current–time product settings (0.5–10.0 mAs) and two tube voltage selections (56 and 70 kVp) were employed. Two pediatric radiologists evaluated 920 images for fracture by using a five-point Likert scale. Area under the receiver operating characteristic curve (A_z) values for the imaging systems were compared by using nonparametric χ^2 tests (all $P < .05$).

Results: For pooled rater data, performance of computed radiography was comparable to that of screen-film imaging, and superior performance ($P = .04$) was achieved with the more experienced rater. The A_z value tended to increase as the tube current–time product setting was increased. Within each system, there was no significant difference in A_z values for all images obtained at 56 and 70 kVp (dual-side–read IP, $P = .63$; single-side–read IP, $P = .25$; screen-film imaging system, $P = .5$). At 56 kVp, a dose reduction of up to 69% was achieved, and accuracy of computed radiography was comparable to that of screen-film imaging.

Conclusion: Findings in this study suggest that computed radiography can replace screen-film imaging in the detection of CMLs and may permit dose reduction.

[1] From the Department of Radiology (P.L.K., K.J.S., R.H.C., J.M.P., P.K.K.), Department of Orthopaedics (D.Z.), and Clinical Research Program (K.H.Z.), Children's Hospital Boston, 300 Longwood Ave, Boston, MA 02115; and SPSS, Chicago, Ill (D.P.N.). From the 2006 RSNA Annual Meeting. Received May 9, 2007; revision requested July 10; revision received September 5; accepted September 27; final version accepted October 8. **Address correspondence to** P.K.K. (e-mail: *paul.kleinman@childrens.harvard.edu*).

Imaging of suspected inflicted injuries in infants is a demanding task. The American College of Radiology and the American Academy of Pediatrics recommend the use of high-detail screen-film imaging systems for optimal detection of subtle high-specificity indicators such as rib fractures and classic metaphyseal lesions (CMLs) (1–3). The CML is a fracture with distinctive radiologic and histopathologic features that is frequently encountered in abused infants (1,4,5). The diagnostic superiority of these traditional systems has been achieved at the cost of a substantial increase in radiation exposure (2). Findings in numerous studies suggest that, despite its lower spatial resolution, digital radiography has the potential to replace screen-film imaging in rigorous skeletal applications (6–31), but there are limited data in regard to the use of this modality for evaluation of inflicted skeletal injuries in infants (32–34). At U.S. pediatric health care facilities, most skeletal survey examinations in infants suspected of being abused are performed with computed radiography; however, there are no specific guidelines for optimizing diagnostic performance while keeping radiation exposure as low as reasonably achievable (35,36). Thus, the purpose of our study was to prospectively determine in a fetal pig model whether diagnostic performance comparable to that of high-detail screen-film imaging can be achieved with computed radiography for the detection of simulated CMLs, by using Faxitron digital images as the reference standard, and whether radiation dose reduction is possible.

Advances in Knowledge

- Computed radiography provides diagnostic performance comparable to that of high-detail screen-film imaging for the detection of simulated classic metaphyseal lesions in a fetal pig model.
- The radiation dose from traditional high-detail screen-film imaging can be reduced by using computed radiography without significant loss of diagnostic performance.

Materials and Methods

This study received financial support and equipment from Fuji, Stamford, Conn. The authors had control over the information and data submitted for this publication. This study was granted exempt status by the institutional review board and animal care and use committee because of the use of commercially available frozen deceased fetal pigs.

Fetal Pig Model

The femur of the late-gestational fetal pig was chosen because of its morphologic similarities to that of the human infant (37,38). The hind legs of 20 previously frozen deceased near-term mixed-breed fetal pigs (Pel-Freeze Arkansas, Biologicals Division, Rogers, Ark) that ranged in weight from 0.93–1.60 kg (mean, 1.25 kg) were surgically removed (P.L.K.), with muscle, surrounding soft tissue, and skin retained to generate absorption and scatter radiation conditions similar to those of the femur and lower leg of an infant. A coin was tossed to determine which femur (right or left) would be used as the control femur (Fig 1). The 20 contralateral knee joints were subjected to manual varus and/or valgus stresses in an extended position (P.L.K.) to create metaphyseal fractures in the distal femurs in a manner similar to that described by O'Connor et al (39). If a fracture bore similarity to a CML, the femur was entered into the imaging chain. If the fracture was not suitable or had unacceptable overlying artifact, the femur was removed from the study ($n = 3$). In the latter situation, the previously imaged control femur from the same fetal pig was stressed to create a fracture. There were thus 20 fractures (nine right, 11 left) and 20 control femurs (12 right, eight left). After documentation (as mentioned later), fractures were grouped according to four grades of conspicuity. In grade 1, fractures were very inconspicuous ($n = 2$); in grade 2, fractures were inconspicuous ($n = 9$); in grade 3, fractures were conspicuous ($n = 5$); and in grade 4, fractures were very conspicuous ($n = 4$) (Fig 2). Fractures were grouped by two nonrater authors (P.K.K., P.L.K., with 30 and 20 years of experience, respectively, in pediatric imaging) in consensus.

Fracture Documentation: Reference Standard

Each hind leg was imaged in the anteroposterior projection with the x-ray beam centered over the knee joint (average thickness, 2.54 cm). A calibrated Faxitron digital imaging camera (model MX-20; Faxitron X-Ray, Wheeling, Ill) with a 20-μm nominal focal spot and a spatial resolution of 10 line pairs per millimeter was used to document the presence of fractures (P.K.K., P.L.K.) by using a radiographic technique with 6.0 mAs at 32 kVp. Fractures were further documented by using a direct-exposure film packet (Kodak TL; Eastman Kodak, Rochester, NY) with a spa-

Implication for Patient Care

- Computed radiography offers potential dose reduction compared with the dose from traditional high-detail screen-film imaging in skeletal surveys for cases of suspected infant abuse.

Published online before print
10.1148/radiol.2472070811

Radiology 2008; 247:381–390

Abbreviations:
A_z = area under the ROC curve
CML = classic metaphyseal lesion
DQE = detective quantum efficiency
IP = imaging plate
ROC = receiver operating characteristic

Author contributions:
Guarantor of integrity of entire study, P.L.K.; study concepts/study design or data acquisition or data analysis/interpretation, all authors; manuscript drafting or manuscript revision for important intellectual content, all authors; manuscript final version approval, all authors; literature research, P.L.K., D.Z., K.H.Z., P.K.K.; experimental studies, P.L.K., D.Z., K.J.S., R.H.C., J.M.P., P.K.K.; statistical analysis, P.L.K., D.Z., D.P.N., K.H.Z., P.K.K.; and manuscript editing, all authors

See Materials and Methods for pertinent disclosures.

tial resolution of more than 20 line pairs per millimeter. These images were acquired at 250 mAs and 56 kVp with the same portable x-ray unit used for the study images, as indicated later.

Study Radiographic Equipment and Techniques

A single calibrated portable x-ray unit, with a 0.75-mm nominal focal spot size and a nominal tube current of 100 mA (AMX 4; GE Healthcare, Milwaukee, Wis) was used for all study imaging. The half-value layer of the x-ray tube was measured at 2.16 mm aluminum (Al) at 60 kVp and 2.84 mm Al at 80 kVp by using a triad electrometer (Keithley Instruments, Cleveland, Ohio) with a 15-cm^3 ionization chamber and type 1100 Al filter (Fluke Biomedical, Cleveland, Ohio).

Each hind leg was imaged on a tabletop (collimation field size, 8.3 × 14.6 cm) in the anteroposterior projection at a source-to-image distance of 101.6 cm (source-to-skin entrance, 99.1 cm). The x-ray beam was centered over the knee joint, and the resultant image included the entire hind leg. Computed radiographic images were cropped at postprocessing, and screen-film images were manually framed to display only the femur. All images were acquired at 56 and 70 kVp. Computed radiographic images were obtained at tube current–time product settings of 0.5, 1.0, 2.0, 4.0, 8.0, and 10.0 mAs. The 10.0-mAs setting was used only at 56 kVp with the high-resolution imaging plate (IP) to assure maximal range of exposure. Screen-film images were acquired at 6.4 mAs for 56 kVp, and 2.5 mAs for 70 kVp (total tube current–time product settings, eight). Thus, there were a total of 1320 images in our study (two tube voltage settings multiplied by three computed radiographic IPs multiplied by five tube current–time product settings = 30 images, plus one additional high-resolution IP image [as noted previously] = 31 images, plus the product of one screen-film image multiplied by two tube voltage settings = 33 images multiplied by 40 femurs [20 control femurs, 20 femurs with a fracture] = 1320 images). The results of evaluation with screen-film imaging and standard and high-resolution computed radiographic IPs (920 images) are reported in this article. The results of the study of the hybrid computed radiographic IP (400 images) will be reported separately. Air kerma was measured with the same electrometer and 15-cm^3 ionization chamber previously mentioned (Table 1).

Computed Radiographic Imaging

All fractures were imaged with standard (ST-VI; Fuji, Stamford, Conn), high-resolution (HR-BD; Fuji, Stamford, Conn), and hybrid (ST-BD; Fuji, Stamford, Conn) IPs. With the 8 × 10-inch standard IP, a standard-thickness phosphor layer is used with a full light-occluding backing material (40). Light emitted from the phosphor during laser readout is collected from the front side of the IP

Figure 1

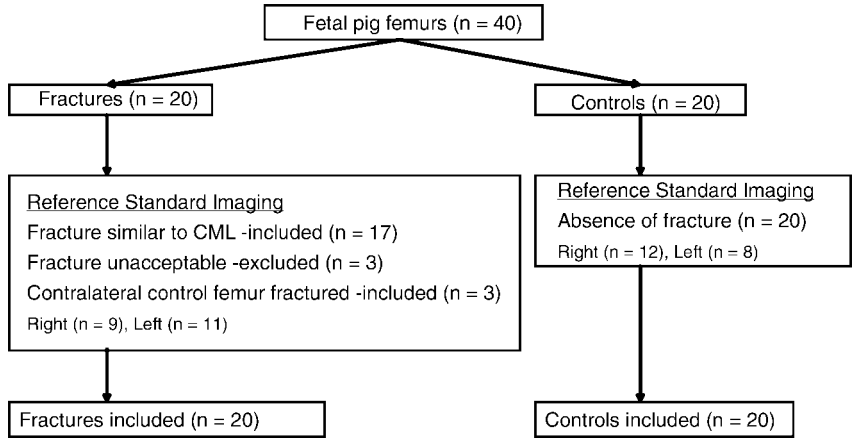

Figure 1: Flow diagram of reference standard determination.

Figure 2

a. **b.**

Figure 2: Anteroposterior Faxitron digital images of fractures (arrows). **(a)** Grade 1 metaphyseal fracture arising from lateral aspect of distal left femur in 1.5-kg fetal pig. **(b)** Grade 4 metaphyseal fracture arising from medial aspect of distal left femur in 1.2-kg fetal pig.

only. With the 18 × 24-cm high-resolution IP, a thinner phosphor layer mounted on an optically clear backing material, which permits dual-side collection of emitted light, is used. This dual-side–read computed radiographic technology results in improved overall efficiency compared with the single-side–read IP (41–45). A calibrated computed radiographic reader (Fujifilm 5000 MA Plus; Fuji) with the capability of single- and dual-side reading was used to process the computed radiographic IPs. This reader is similar to the multiplate reader (ClearView C-S; Fuji) commercially available in the United States. The high-resolution IP was read with 50-μm pixel sampling (3540 × 4740 pixels), a superior spatial resolution compared with the 100-μm pixel sampling (2000 × 2510 pixels) of the standard IP (Fig 3). The hybrid IP also has the capability of dual-side reading with 50-μm pixel sampling, and results obtained with this IP, as noted previously, will be reported separately.

A computed radiographic pediatric (0–3 years) hand-processing menu (Fuji Photo Film, Tokyo, Japan) was selected and tailored with gradation-processing parameters (rotation amount, 1.2; gradation type, O; rotation center, 0.6; and density shift, 0.25) and multiobjective frequency-processing parameters (multifrequency-balance type, C; multifrequency-enhancing type, T; degree of multifrequency enhancement, 1.0; multidynamic range control–balance type, A; multidynamic range control–enhancing type, A; and degree of multidynamic range control enhancement, 0) to produce optimal images (46). The latitude number was constant for all images. The sensitivity number varied according to the tube current–time product and tube voltage combination employed. All image identification data were removed from view before rater evaluation.

Images were transmitted from the computed radiographic reader to an IP workstation (FCR XG-1; Fuji) that uses software (FCR, version V2.1 (B); Fuji Photo Film) and a monitor (Dome C2, model C2GRAY; Planar Systems, Waltham, Mass) with a resolution of 1600 × 1280. Images were assessed for appropriate exposure parameters (P.L.K.), collimated, and sent via Digital Imaging and Communications in Medicine transfer to a picture archiving and communication system equipped with software (Synapse, version 3.1.1; Fuji) with Joint Photographic Experts Group lossless storage (compression rate, two to one) before evaluation.

Table 1

Air Kerma Measured for Each Tube Current–Time Product and Tube Voltage Combination

Tube Current–Time Product (mAs)	Air Kerma with 56 kVp (μGy)	Air Kerma with 70 kVp (μGy)
0.5	11.8	19.9
1.0	23.0	39.9
2.0	44.6	79.3
2.5*	. . .	98.7
4.0	88.7	158
6.4*	142	. . .
8.0	178	315
10.0†	222	. . .

Note.—Measurements were taken at a source-to-detector distance of 99.1 cm.

* Screen-film imaging only.

† High-resolution IP only.

Figure 3

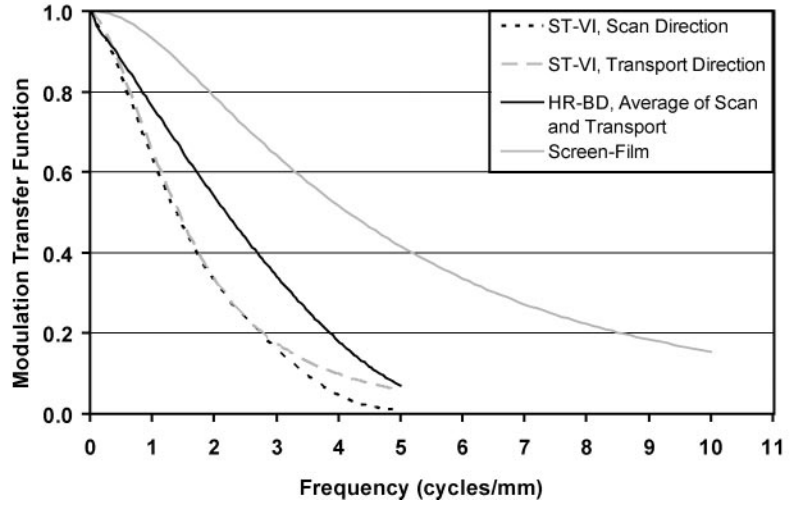

Figure 3: Plot shows presampled modulation transfer function data for standard IP *(ST-VI),* high-resolution IP *(HR-BD),* and screen-film imaging systems. Nyquist frequency for two computed radiographic systems read with 100-μm pixel sampling was five cycles per millimeter. (Computed radiographic data courtesy of Fetterly and Schueler [41,42]. Screen-film imaging data courtesy of Eastman Kodak, Rochester, NY.)

Screen-Film Imaging and Processing

A high-detail (13 line pairs per millimeter), 8 × 10-inch screen-film imaging system with a speed of 50 (InSight Pediatric Ultra Detail screens and InSight Pediatric film; Eastman Kodak) was used to image all femurs. The average optical density of bone was 1.14. Images were developed with a film processor (RP X-OMAT, model M6B; Eastman Kodak).

Image Evaluation

The resultant 1320 images (920 reported here) were randomized and grouped into folders for nine evaluation sessions. One hundred twenty-four (10%) of 1240 computed radiographic images and 40 (50%) of 80 screen-film images were randomly selected for intraobserver reliability. After a test session, two board-certified pediatric radiologists (rater 1 [R.H.C.] and rater 2 [J.M.P.], with 30 and 5 years of experience, respectively) blindly evaluated each image for likelihood (percentage)

Figure 4

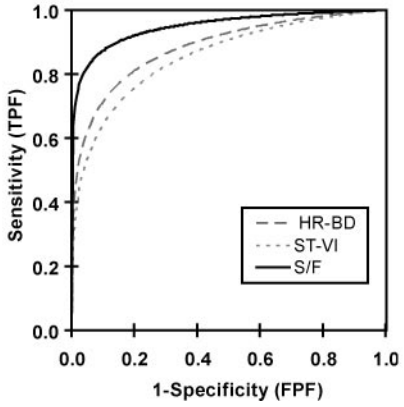

Figure 4: Conventional binormal ROC curves of pooled raters and tube current–time product and tube voltage settings show no significant difference between high-resolution IP *(HR-BD)* ($A_z = 0.85$) and screen-film imaging *(S/F)* ($A_z = 0.90$) ($P = .08$). There is a significant decreased performance of the standard IP *(ST-VI)* ($A_z = 0.82$) compared with screen-film imaging ($P < .01$). *FPF* = false-positive fraction, *TPF* = true-positive fraction.

Table 2

Maximal A_z Values for All Fracture Grades and Pooled Raters at 56 and 70 kVp

Tube Voltage and System	A_z Value*	Tube Current–Time Product (mAs)	Air Kerma (μGy)
With 56 kVp			
High-resolution IP	0.96 ± 0.04†	8.0	178
Standard IP	0.93 ± 0.03†	8.0	178
Screen-film imaging	0.92 ± 0.03†	6.4	142
With 70 kVp			
High-resolution IP	0.92 ± 0.03	8.0	315
Standard IP	0.92 ± 0.03	4.0	158
Screen-film imaging	0.88 ± 0.04	2.5	99

* Data are the mean ± standard error of the mean.

† Best overall values.

of fracture by using a five-point Likert scale (0%, no fracture; 25%, fracture not likely; 50%, fracture somewhat likely; 75%, fracture likely; and 100%, definite fracture). A facilitator was present during image evaluations to record and enter raters' observations with spreadsheet software (Excel, version 11.0, 2003; Microsoft, Redmond, Wash). The entire rating period lasted 6 weeks and the intraobserver reliability testing immediately followed the initial readings.

Computed radiographic images were viewed with the software that was used with the picture archiving and communication system at a single high-resolution (2560 × 2048) monitor (Dome C5i; Planar Systems) calibrated to a standardized display function for display of gray-scale images (47), with software (VeriLum, version 5.1, and VeriLum Color Dual Probe; ImageSmiths, Kensington, Md). Images were presented with standard window level settings (512 × 1024), and radiologists were allowed to adjust settings and magnify images.

A ×4 magnifying glass was supplied for evaluating screen-film images at a single view box with an average luminance of 4370 candela (cd)/m^2 (S & S X-Ray Products, Brooklyn, NY). All images were evaluated in the same location with ambient light reduced to less than 25 lux. A photometer was used for light measurements (J-17; Tektronics, Beaverton, Ore).

Statistical Analysis

Rater reliability.—Inter- and intrarater reliability were estimated by using type A (absolute agreement) single-measure intraclass correlation coefficients for a two-way mixed model, with a rated object treated as a random effect and a rater treated as a fixed effect (48).

Detection accuracy and dose reduction.—Receiver operating characteristic (ROC) curves were constructed to measure performance accuracy. Overall accuracy was evaluated with the area under the ROC curve (A_z), estimated by using the nonparametric approximation by using the trapezoidal rule (49). Standard errors, confidence intervals, and differences between A_z values were computed on the basis of the method of DeLong et al (50). A_z values were computed for the various tube current–time product and tube voltage combinations for all imaging systems and were compared for significance with nonparametric χ^2 tests (all $P < .05$). Comparisons among the A_z values were supplemented by modeling these values in a repeated-measures model by using a compound-symmetry covariance structure (51). The mixed modeling of the A_z values was also used to determine the minimum tube current–time product value employed with a computed radiographic system without a significant reduction in A_z compared with that of the screen-film system. Parametric binormal ROC curves were generated by using the maximum likelihood methods that were based on the two estimated ROC parameters (a, b). The estimated parametric A_z was a function of these estimates, where $A_z = \Phi[a/(1 + b^2)^{0.5}]$ and Φ was the cumulative distribution function of a standard normal random variable (49).

Software.—ROC and A_z computations were performed by using statistical software (Stata 9; Stata, College Station, Tex). Mixed modeling of the A_z values was performed by using the Mixed procedure in other software (SPSS, version 14.0; SPSS, Chicago, Ill). Binormal ROC parameters were estimated by using additional software (S-Plus, version 6.2; Insightful, Seattle, Wash). Parametric ROC curves were constructed by using PlotROC.xls, a macro sheet for plotting smooth ROC curves (Excel 5.0; Microsoft), which is available at *http://xray.bsd.uchicago.edu/krl/roc_soft.htm* (Kurt Rossman Laboratories for Radiologic Image Research, University of Chicago, Chicago, Ill). Spreadsheet software mentioned before was used to construct presampled modulation transfer function and potential dose reduction graphs.

Results

Rater Reliability

The intraclass correlation coefficient for intrarater reliability averaged across all

three systems was 0.80 for rater 1 and 0.72 for rater 2. The absolute-agreement intraclass correlation coefficients for interrater reliability were as follows: For high-resolution IP, the intraclass correlation coefficient was 0.77 (95% confidence interval: 0.72, 0.80). For standard IP, it was 0.72 (95% confidence interval: 0.67, 0.76). For screen-film imaging, it was 0.81 (95% confidence interval: 0.72, 0.88).

Figure 5

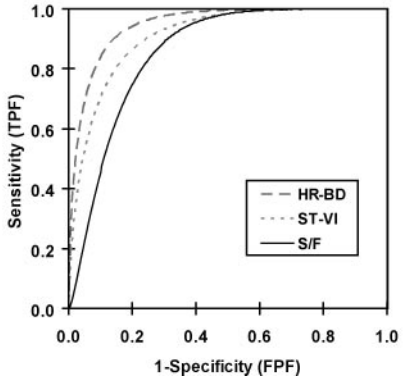

Figure 5: Conventional binormal ROC curves of maximal A_z values for pooled raters and all fracture grades for high-resolution IP, standard IP, and screen-film imaging systems with 56 kVp. No significant differences between systems (high-resolution IP vs standard IP, $P = .17$; high-resolution IP vs screen-film imaging, $P = .2$; standard IP vs screen-film imaging, $P = .72$). Keys are the same as for Figure 4.

Detection Accuracy

When results were pooled for raters and tube voltage and tube current–time product settings, the overall performance of the high-resolution IP was comparable to the overall performance of the screen-film imaging system ($P = .08$) (Fig 4). However, there was a significant decrease in the overall performance of the standard IP when it was compared with the performance of the screen-film system ($P < .01$).

Maximal A_z values and corresponding optimal tube current–time product settings for each system at 56 and 70 kVp pooled for raters and all fracture grades (Table 2) showed that the best overall A_z values for the three imaging systems were achieved at 56 kVp (Fig 5). At 56 kVp, there was a 4% ($A_z = 0.96$ vs 0.92) increase in diagnostic performance for the high-resolution IP when compared with performance of screen-film imaging; however, paired comparisons of these data showed no significant differences (high-resolution IP vs standard IP, $P = .17$; high-resolution IP vs screen-film imaging, $P = .20$; standard IP vs screen-film imaging, $P = .72$). Similarly, at 70 kVp, there were no significant differences for paired comparisons (high-resolution IP vs standard IP, $P = .99$; high-resolution IP vs screen-film imaging, $P = .23$; standard IP vs screen-film imaging, $P = .31$). Note that the performance of the standard IP was identical to the performance of the high-resolution IP at 70 kVp.

Analysis of maximal A_z values and corresponding optimal tube current–time product settings at 56 and 70 kVp that were pooled for raters and were limited to less conspicuous fractures (grades 1 and 2) (Table 3) showed that the best overall A_z values were achieved at 56 kVp for the high-resolution IP, followed by the standard IP at 70 kVp and then the screen-film imaging system at 56 kVp. Paired comparisons showed no significant differences (high-resolution IP vs standard IP, $P = .55$; high-resolution IP vs screen-film imaging, $P = .24$; standard IP vs screen-film imaging, $P = .46$). Data segregated according to tube voltage showed no significant differences at 56 kVp (high-resolution IP vs standard IP, $P = .17$; high-resolution IP vs screen-film imaging, $P = .24$; standard IP vs screen-film imaging, $P = .69$) or at 70 kVp (high-resolution IP vs standard IP, $P = .6$; high-resolution IP vs screen-film imaging, $P = .14$; standard IP vs screen-film imaging, $P = .11$). Note that the performance of all systems was decreased for inconspicuous fractures when compared with all fracture grades (Table 2). The decrease in performance for the high-resolution IP between 56 and 70 kVp did not occur with the standard IP, despite a reduction in dose from 178 to 158 μGy (11%).

The previously mentioned analyses for maximal A_z values were repeated with data segregated according to rater. For the more experienced rater 1 (Table 4), there was a borderline significantly increased performance for high-resolution IP compared with screen-film imaging ($P = .06$) for all fracture grades combined (Fig 6). There was no significant difference between the high-resolution IP and the standard IP ($P = .3$). For rater 2, there were no significant differences for the same analyses (high-resolution IP $A_z = 0.95$ vs standard IP $A_z = 0.91$, $P = .5$; high-resolution IP vs screen-film $A_z = 0.92$, $P = .33$). When these analyses were performed for the less conspicuous fractures (grades 1 and 2) (Table 4), rater 1 performed significantly better with the high-resolution

Table 3

Maximal A_z Values for Fracture Grades 1 and 2 for Pooled Raters at 56 and 70 kVp

Tube Voltage and System	A_z Value*	Tube Current–Time Product (mAs)	Air Kerma (μGy)
With 56 kVp			
High-resolution IP	0.92 ± 0.04†	8.0	178
Standard IP	0.88 ± 0.05	8.0	178
Screen-film imaging	0.86 ± 0.05†	6.4	142
With 70 kVp			
High-resolution IP	0.87 ± 0.05	8.0	315
Standard IP	0.89 ± 0.04†	4.0	158
Screen-film imaging	0.79 ± 0.06	2.5	99

* Data are the mean ± standard error of the mean.

† Best overall values.

IP than with screen-film imaging (P = .04) (Fig 7). There was no significant difference between the standard IP and screen-film imaging (P = .1). For rater 2, there were no significant differences for the same analyses (high-resolution IP A_z = 0.90 vs screen-film imaging A_z = 0.85, P = .33; standard IP A_z = 0.86 vs screen-film imaging A_z = 0.85, P = .92).

There was a trend for improved performance with increasing tube current–time product setting (Table 5). For the standard IP, pooled rater predicted A_z increased at tube current–time product settings between 0.5 and 4.0. For the high-resolution IP, the predicted A_z increased at tube current–time product settings between 0.5 and 8.0. By using pooled tube current–time product and rater data, there was no significant difference in performance between 56 and 70 kVp settings, respectively, within each system: For high-resolution IP, A_z = 0.86 vs A_z = 0.85 (P = .63). For standard IP, A_z = 0.84 vs A_z = 0.81 (P = .25). For screen-film imaging, A_z = 0.92 vs A_z = 0.88 (P = .5).

Dose Reduction

Results of the mixed-model analysis demonstrated the potential for radiation dose reduction by using computed radiography, compared with screen-film imaging, and was most evident at 56 kVp (Fig 8). The tube current–time product of 6.4 mAs that was used with the screen-film imaging system could be reduced to 4.0 mAs with the high-resolution IP, and this reduction resulted in a dose reduction of 38% (2.4 of 6.4), with no significant difference in performance (high-resolution IP A_z = 0.90 vs screen-film imaging A_z = 0.92, P < .001). The standard IP tube current–time product setting could be reduced to 2.0, and this reduction resulted in a dose reduction of 69% (4.4 of 6.4), again with no significant difference in performance (standard IP A_z = 0.90 vs screen-film imaging A_z = 0.92, P < .001).

Table 4

Maximal A_z Values for All Fracture Grades Combined and Fracture Grades 1 and 2 Only for Rater 1

System	A_z Value for All Fractures*	A_z Value for Fracture Grades 1 and 2*	Tube Current–Time Product (mAs)	Tube Voltage (kVp)	Air Kerma (μGy)
High-resolution IP	0.98 ± 0.02	0.96 ± 0.03	8.0	56	178
Standard IP	0.96 ± 0.03	0.94 ± 0.04	4.0	70	158
Screen-film imaging	0.90 ± 0.05	0.85 ± 0.08	6.4	56	142

* Data are the mean ± standard error of the mean.

Figure 6

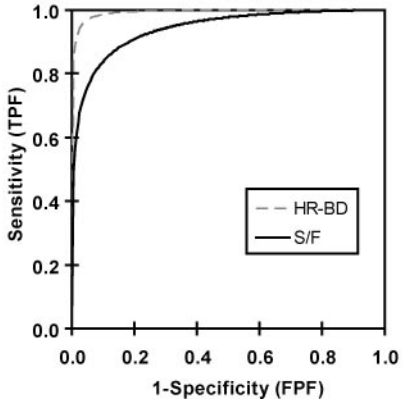

Figure 6: Conventional binormal ROC curves of maximal A_z values for rater 1 and all fracture grades with 56 kVp. There is borderline significant increased performance of high-resolution IP (A_z = 0.98) compared with screen-film imaging (A_z = 0.90) (P = .06). Keys are the same as for Figure 4.

Figure 7

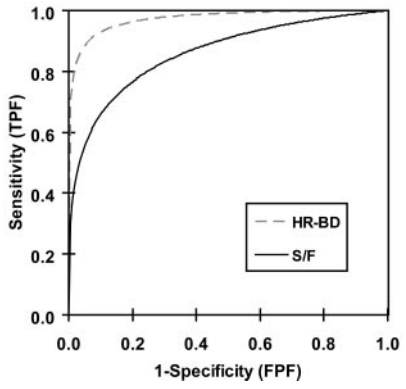

Figure 7: Conventional binormal ROC curves of maximal A_z values for rater 1 and fracture grades 1 and 2 with 56 kVp. There is significant increased performance of high-resolution IP (A_z = 0.96) compared with screen-film imaging (A_z = 0.85) (P = .04). Keys are the same as for Figure 4.

Discussion

Overall, we found that computed radiography was comparable to or superior to high-detail screen-film imaging. The statistical superiority of screen-film imaging over the standard IP can be explained by the pooled data (all tube current–time product and tube voltage combinations) in this overall performance analysis. A more clinically relevant approach to system comparisons was achieved by comparing the maximal performance (single combination of tube current–time product and tube voltage) of each imaging system. By using this method, both the high-resolution and the standard IPs consistently outperformed the screen-film imaging system for pooled raters; however, these differences were not significant. When data were segregated according to rater and fracture conspicuity grades, an interesting pattern emerged. In the hands of the more experienced rater 1, the high-resolution IP outperformed the screen-film imaging system, with borderline significance when all fractures were evaluated. This superior performance rose to statistical significance when only low-conspicuity fractures were evaluated. This suggests that, for the more experienced rater, the high-resolution IP provided certain advantages that permitted discrimination between fractured and normal bones. This significantly better

performance was not observed in the comparison between the standard IP and screen-film imaging systems. Although we did not observe a significantly superior performance of high-resolution IP when it was compared with standard IP, it is notable that the high-resolution computed radiographic system compared more favorably with traditional screen-film imaging than did the standard computed radiographic system.

These findings confirm those of others that, despite its lower spatial resolution, computed radiography has performance that is comparable to that of screen-film imaging in skeletal applications (6,7,14,21,24). This improved performance relates to the higher contrast resolution of computed radiography versus that of screen-film imaging. The linear response of the computed radiographic plate over a wide range of exposures and the broad dynamic range of this system yield high contrast resolution. On the other hand, screen-film imaging systems are limited by a narrow range of exposure (latitude) and a nonlinear response (15). Although the modulation transfer function curves of the high-resolution and standard IPs are well to the left of the curve of the screen-film imaging system, reflecting their lower spatial resolution (Fig 2), comparable performance of these systems was achieved in this study.

The trend toward superior performance of the high-resolution IP versus the standard IP relates to the higher detective quantum efficiency (DQE) of the dual-side–read high-resolution IP. The DQE improves with increased spatial resolution (as measured by the modulation transfer function) and decreases with an increase in system noise, as measured by the noise power spectrum. Collection of data from both sides of the high-resolution IP results in improved signal-to-noise ratio compared with the collection of data from the single-side–read standard IP. The resultant decreased noise power spectrum translates into improved DQE of the dual-side–read IP (41–44). In addition, the high-resolution IP is sampled at a 50-μm pixel rate, affording higher spatial resolution compared with that at the 100-μm pixel rate of the standard IP. Although our data fail to prove diagnostic superiority of high-resolution computed radiography compared with standard computed radiography in this experimental model, the trend toward improved performance of the high-resolution IP lends support to the use of a computed radiographic imaging system with a superior DQE for the demanding application of subtle inflicted skeletal injuries.

An important finding in our study was the relationship between tube current–time product setting and diagnostic performance, a pattern most evident at 56 kVp (Table 5). For the standard IP, we found that, as the tube current–time product setting increased from 0.5 to 4.0, there was a progressive increase in A_z. This relationship toward increased performance extended to settings of 8.0 mAs for the high-resolution IP. This trend is in keeping with the relationship between system noise and DQE discussed before. In general, within a specified computed radiographic IP exposure range, system noise decreases with increasing tube current–time product. Several studies have demonstrated the relationship between tube current–time product setting and diagnostic performance by using computed radiography in skeletal examinations (13,14). Our study goes beyond these earlier works by using blinded assessments of multiple fractures on images with varying conspicuity acquired with high-resolution computed radiography and screen-film imaging with a range of tube current–time product and tube voltage combinations. We believe our results provide a compelling argument for appropriate radiographic exposure factors to optimize system performance for the detection of subtle skeletal injury.

In the screen-film imaging era, it was customary to employ a relatively low tube voltage for rigorous skeletal

Table 5

Tube Current–Time Product versus A_z Pooled Rater Data for All Fracture Grades

Tube Voltage, System, and Tube Current–Time Product (mAs)	A_z Value	Predicted A_z Value*
With 56 kVp		
High-resolution IP		
0.5	0.75	0.75 ± 0.03
1.0	0.80	0.77 ± 0.03
2.0	0.79	0.82 ± 0.03
4.0	0.90	0.89 ± 0.03
8.0	0.96	0.95 ± 0.03
10.0	0.95	0.95 ± 0.04
Standard IP		
0.5	0.75	0.73 ± 0.03
1.0	0.75	0.77 ± 0.03
2.0	0.90	0.84 ± 0.03
4.0	0.88	0.94 ± 0.03
8.0	0.93	0.93 ± 0.04
With 70 kVp		
High-resolution IP		
0.5	0.81	0.78 ± 0.03
1.0	0.77	0.80 ± 0.03
2.0	0.81	0.83 ± 0.03
4.0	0.89	0.88 ± 0.03
8.0	0.92	0.91 ± 0.03
Standard IP		
0.5	0.66	0.72 ± 0.03
1.0	0.80	0.75 ± 0.03
2.0	0.80	0.82 ± 0.03
4.0	0.92	0.89 ± 0.03
8.0	0.85	0.84 ± 0.04

* Data are the mean ± standard error of the mean, based on the mixed model.

Figure 8

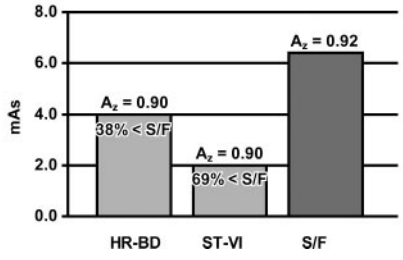

Figure 8: Graph shows potential dose reduction at 56 kVp for pooled raters and all fracture grades. Mixed-model analysis results show the minimum tube current–time product value and percentage of dose reduction achievable by using high-resolution IP and standard IP without a significant decrease in A_z when compared with screen-film imaging (high-resolution IP vs screen-film imaging and standard IP vs screen-film imaging, $P < .001$). Keys are the same as for Figure 4.

radiographic applications to achieve high-contrast images. Through proper selection of image processing and display parameters, digital imaging may permit high-contrast skeletal imaging acquisition at higher tube voltage settings (7,52). We found it encouraging that there was no significant difference in the overall diagnostic performance with images acquired at 56 and 70 kVp. Our findings support the view that digital skeletal imaging may have the potential to operate in a higher tube voltage range than does screen-film imaging.

We found that the maximal diagnostic performance of the two digital systems was achieved at doses greater than the dose employed for the high-detail screen-film imaging system. To reduce this dose, the mixed-model analysis was performed to determine the minimum tube current–time product setting that could be used with computed radiography while maintaining diagnostic performance comparable to that of screen-film imaging. The 38% and 69% reductions in tube current–time product with the high-resolution and standard IPs, respectively, at 56 kVp provide support for the view that dose reduction is possible with this computed radiographic application. However, because a decrease in IP exposure is accompanied by an increase in image noise, efforts to reduce dose must be carefully scrutinized to strike an appropriate balance between radiation dose and diagnostic performance. Technical innovations in computed radiography, as well as in flat-panel–based digital systems, offer promise of higher DQEs, permitting dose reduction with maintenance or improvement in diagnostic performance when compared with high-detail screen-film imaging (11–15,17,20–23,26,27, 29,34,45,53–56).

There were several limitations to our study. First, the smaller femurs of the fetal pigs in this study compared with human infant femurs may have resulted in less conspicuous fractures than those commonly encountered in clinical practice (5,57). Therefore, the rigor required for fracture detection in this experimental model may have been greater than that in the customary diagnostic setting. In addition, an inherent limitation in a study in which analog images are compared with digital images is that raters may be biased because they have knowledge as to which image acquisition method was employed. Last, because our study employed only two tube voltage settings and it also did not permit acquisition and comparison of the images obtained with 56 and 70 kVp at identical radiation doses, we were unable to fully assess the influence of tube voltage on diagnostic performance. Further studies will be required in this regard.

Practical application: Our study findings suggest that computed radiography can replace traditional high-detail screen-film imaging for the detection of inflicted skeletal injuries in infants and offer the prospect of substantial dose reduction. Although most pediatric health care facilities in the United States have migrated to computed radiography for imaging in cases in which an infant is suspected of being abused, computed radiographic systems are frequently not optimized for high-detail skeletal applications (35). Our findings support the recommendation of the American College of Radiology that an increase in the tube current–time product setting that is higher than that used for general pediatric applications may be required for optimal detection of skeletal injuries (2). This strategy for a special approach to infant skeletal surveys acquired with computed radiography mirrors the use of a high-detail imaging system in the screen-film imaging era. Departments should carefully select their computed radiographic or other digital systems with particular attention to high diagnostic efficiency and optimize technical factors and processing parameters suitable to this demanding imaging application. Failure to optimize computed radiography for infant skeletal surveys may result in missed cases of inflicted injury. An enlightened approach to this challenge may result in considerable dose reduction compared with the dose for traditional high-detail screen-film imaging.

Acknowledgments: The authors thank Patricia Dunning, RT (R), for her technical assistance and Susan L. Ivey, MBA, for help in preparation of the manuscript.

References

1. Kleinman PK, Marks SC, Blackbourne B. The metaphyseal lesion in abused infants: a radiologic-histopathologic study. AJR Am J Roentgenol 1986;146:895–905.
2. American College of Radiology. ACR practice guideline for skeletal surveys in children (Res. 47, 17, 35). In: ACR Standards. Reston, Va: American College of Radiology, 2006; 145–149.
3. Diagnostic imaging of child abuse. Pediatrics 2000;105:1345–1348.
4. Caffey J. Some traumatic lesions in growing bones other than fractures and dislocations: clinical and radiological features—the Mackenzie Davidson Memorial Lecture. Br J Radiol 1957;30:225–238.
5. Kleinman PK, Marks SC Jr, Richmond JM, Blackbourne BD. Inflicted skeletal injury: a postmortem radiologic-histopathologic study in 31 infants. AJR Am J Roentgenol 1995;165:647–650.
6. Wilson AJ, Mann FA, West OC, McEnery KW, Murphy WA Jr. Evaluation of the injured cervical spine: comparison of conventional and storage phosphor radiography with a hybrid cassette. Radiology 1994;193:419–422.
7. Prokop M, Galanski M, Oestmann JW, et al. Storage phosphor versus screen-film radiography: effect of varying exposure parameters and unsharp mask filtering on the detectability of cortical bone defects. Radiology 1990;177:109–113.
8. Ludwig K, Henschel A, Bernhardt TM, et al. Performance of a flat-panel detector in the detection of artificial erosive changes: comparison with conventional screen-film and storage-phosphor radiography. Eur Radiol 2003;13:1316–1323.
9. Wilson AJ, Mann FA, Murphy WA Jr, Monsees BS, Linn MR. Photostimulable phosphor digital radiography of the extremities: diagnostic accuracy compared with conventional radiography. AJR Am J Roentgenol 1991;157:533–538.
10. Ludwig K, Link TM, Fiebich M, et al. Selenium-based digital radiography in the detection of bone lesions: preliminary experience with experimentally created defects. Radiology 2000;216:220–224.
11. Ludwig K, Schulke C, Diederich S, et al. Detection of subtle undisplaced rib fractures in a porcine model: radiation dose requirement—digital flat-panel versus screen-film and storage-phosphor systems. Radiology 2003;227:163–168.
12. Ludwig K, Lenzen H, Kamm KF, et al. Performance of a flat-panel detector in detecting artificial bone lesions: comparison with conventional screen-film and storage-phosphor radiography. Radiology 2002;222:453–459.
13. Seifert H, Kubale R, Hagen T, Kramann B, Leetz HK. A study of dose reduction using digital luminescence radiography for lateral skull radiography. Br J Radiol 1996;69:311–317.
14. Peer R, Lanser A, Giacomuzzi SM, et al. Storage phosphor radiography of wrist fractures: a subjective comparison of image quality at varying exposure levels. Eur Radiol 2002;12:1354–1359.
15. Kottamasu SR, Kuhns LR, Stringer DA. Pediatric musculoskeletal computed radiography. Pediatr Radiol 1997;27:563–575.

16. Murphey MD, Quale JL, Martin NL, Bramble JM, Cook LT, Dwyer SJ 3rd. Computed radiography in musculoskeletal imaging: state of the art. AJR Am J Roentgenol 1992;158:19–27.

17. Ludwig K, Ahlers K, Wormanns D, et al. Lumbar spine radiography: digital flat-panel detector versus screen-film and storage-phosphor systems in monkeys as a pediatric model. Radiology 2003; 229:140–144.

18. Murphey MD, Bramble JM, Cook LT, Martin NL, Dwyer SJ 3rd. Nondisplaced fractures: spatial resolution requirements for detection with digital skeletal imaging. Radiology 1990;174:865–870.

19. Murphey MD. Digital skeletal radiography: spatial resolution requirements for detection of subperiosteal resorption. AJR Am J Roentgenol 1989; 152:541–546.

20. Zähringer M, Krug B, Kamm KF, et al. Detection of porcine bone lesions and fissures: comparing digital selenium, digital luminescence, and analog film-screen radiography. AJR Am J Roentgenol 2001;177:1397–1403.

21. Phillips JH, Albregts AE, Kling TF Jr, Cohen MJ. Digital radiography in pediatric orthopaedics: a prospective, controlled, and randomized trial. J Pediatr Orthop 1994;14:377–380.

22. Strotzer M, Gmeinwieser J, Spahn M, et al. Amorphous silicon, flat-panel, x-ray detector versus screen-film radiography: effect of dose reduction on the detectability of cortical bone defects and fractures. Invest Radiol 1998;33:33–38.

23. Strotzer M, Völk M, Wild T, von Landenberg P, Feuerbach S. Simulated bone erosions in a hand phantom: detection with conventional screen-film technology versus cesium iodide-amorphous silicon flat-panel detector. Radiology 2000;215:512–515.

24. Swee RG, Gray JE, Beabout JW, et al. Screen-film versus computed radiography imaging of the hand: a direct comparison. AJR Am J Roentgenol 1997;168:539–542.

25. Uffmann M, Schaefer-Prokop C, Neitzel U, Weber M, Herold CJ, Prokop M. Skeletal applications for flat-panel versus storage-phosphor radiography: effect of exposure on detection of low-contrast details. Radiology 2004;231:506–514.

26. Völk M, Paetzel C, Angele P, et al. Routine skeleton radiography using a flat-panel detector: image quality and clinical acceptance at 50% dose reduction. Invest Radiol 2003;38:230–235.

27. Völk M, Strotzer M, Holzknecht N, et al. Digital radiography of the skeleton using a large-area detector based on amorphous silicon technology: image quality and potential for dose reduction in comparison with screen-film radiography. Clin Radiol 2000;55:615–621.

28. Jónsson A, Borg A, Hannesson P, et al. Film-screen vs. digital radiography in rheumatoid arthritis of the hand: an ROC analysis. Acta Radiol 1994;35:311–318.

29. Jónsson A, Laurin S, Karner G, et al. Spatial resolution requirements in digital radiography of scaphoid fractures: an ROC analysis. Acta Radiol 1996;37:555–560.

30. Langen HJ, Klein HM, Wein B, Stargardt A, Gunther RW. Comparative evaluation of digital radiography versus conventional radiography of fractured skulls. Invest Radiol 1993;28:686–689.

31. Pettersson H, Aspelin P, Boijsen E, Herrlin K, Egund N. Digital radiography of the spine, large bones and joints using stimulable phosphor: early clinical experience. Acta Radiol 1988;29:267–271.

32. Kleinman PK, O'Connor B, Nimkin K, et al. Detection of rib fractures in an abused infant using digital radiography: a laboratory study. Pediatr Radiol 2002;32:896–901.

33. Offiah AC, Moon L, Hall CM, Todd-Pokropek A. Diagnostic accuracy of fracture detection in suspected non-accidental injury: the effect of edge enhancement and digital display on observer performance. Clin Radiol 2006;61:163–173.

34. Offiah AC, Grehan J, Hall CM, Todd-Pokropek A. Optimal exposure parameters for digital radiography of the infant skull: a pilot study. Clin Radiol 2005;60: 1195–1204.

35. Kleinman PL, Kleinman PK, Savageau JA. Suspected infant abuse: radiographic skeletal survey practices in pediatric health care facilities. Radiology 2004;233:477–485.

36. Roehrig H, Krupinski EA, Hulett R. Reduction of patient exposure in pediatric radiology. Acad Radiol 1997;4:547–557.

37. Connolly SA, Jaramillo D, Hong JK, Shapiro F. Skeletal development in fetal pig specimens: MR imaging of femur with histologic comparison. Radiology 2004;233:505–514.

38. Wrathall AE, Bailey J, Hebert CN. A radiographic study of development of the appendicular skeleton in the fetal pig. Res Vet Sci 1974;17:154–168.

39. O'Connor SC, Ruess L, Quinn WJ, Medina LS, Wells CN, Anderson ML. Film screen and computed radiography in the detection of classic metaphyseal lesions in an animal model of child abuse [abstr]. Pediatr Radiol 2003;33(suppl 1): S101.

40. Kengyelics SM, Davies AG, Cowen AR. A comparison of the physical imaging properties of Fuji ST-V, ST-VA, and ST-VN computed radiography image plates. Med Phys 1998;25:2163–2169.

41. Fetterly KA, Schueler BA. Performance evaluation of a "dual-side read" dedicated mammography computed radiography system. Med Phys 2003;30:1843–1854.

42. Fetterly KA, Schueler BA. Performance evaluation of a computed radiography imaging device using a typical "front side" and novel "dual side" readout storage phosphors. Med Phys 2006;33: 290–296.

43. Monnin P, Holzer Z, Wolf R, et al. An image quality comparison of standard and dual-side read CR systems for pediatric radiology. Med Phys 2006;33:411–420.

44. Ideguchi T, Higashida Y, Kawaji Y, et al. New CR system with pixel size of 50 micron for digital mammography: physical imaging properties and detection of subtle microcalcifications. Radiat Med 2004;22:218–224.

45. Neitzel U. Status and prospects of digital detector technology for CR and DR. Radiat Prot Dosimetry 2005;114:32–38.

46. Fuji photograph film. In: Fujifilm imaging and information booklet. Tokyo, Japan: Fuji Photo Film, 1999.

47. Digital Imaging and Communications in Medicine (DICOM) part 14: grayscale standard display function. Rosslyn, Va: National Electrical Manufacturers Association, 2007.

48. McGraw KO, Wong SP. Forming inferences about some intraclass correlation coefficients. Psychological Methods 1996;1:30–46.

49. Hanley JA, McNeil BJ. The meaning and use of the area under a receiver operating characteristic (ROC) curve. Radiology 1982;143:29–36.

50. DeLong ER, DeLong DM, Clarke-Pearson DL. Comparing the areas under two or more correlated receiver operating characteristic curves: a nonparametric approach. Biometrics 1988;44: 837–845.

51. Fitzmaurice GM, Laird NM, Ware JH. Applied longitudinal analysis. New York, NY: Wiley, 2004.

52. Hamer OW, Völk M, Zorger Z, Feuerbach S, Strotzer M. Amorphous silicon, flat-panel, x-ray detector versus storage phosphor-based computed radiography: contrast-detail phantom study at different tube voltages and detector entrance doses. Invest Radiol 2003;38:212–220.

53. Broderick NJ, Long B, Dreesen RG, et al. Phosphor plate computed radiography: response to variation in mAs at fixed kVp in an animal model—potential role in neonatal imaging. Clin Radiol 1993;47:39–45.

54. Aldrich JE, Duran E, Dunlop P, Mayo JR. Optimization of dose and image quality for computed radiography and digital radiography. J Digit Imaging 2006;19:126–131.

55. Schreiner-Karoussou A. Dose optimisation in computed radiography. Radiat Prot Dosimetry 2005;117:139–142.

56. Seifert H, Chapot C. Reduction of patient exposure by the use of digital luminescence radiography [in French]. J Radiol 1999;80:1555–1560.

57. Needlman R. Part II. Growth and Development. In: Behrman R, Kliegman R, Jenson H, eds. Nelson textbook of pediatrics. 17th ed. Philadelphia, Pa: Saunders, 2004; 23–66.